

Construction and performance test of charged particle detector array for MATE

X. B. Li^{a,b}, L. H. Ru^{a,b}, Z. C. Zhang^{a,b,*}, B.F. Lv^{a,b}, N. T. Zhang^{a,b,*},
J. L. Zhang^{a,b}, C. G. Lu^{a,b}, B. S. Gao^{a,b}, J. B. Ma^{a,b}, F. S. Shi^{a,b},
S. Terashima^{a,d,e}, X. D. Xu^{a,b}, Z. Bai^a, S. W. Xu^a, Y. Y. Yang^{a,b},
H. J. Ong^{a,b,c,d,e,*}, X. D. Tang^{a,b,c}

^a*Institute of Modern Physics (IMP), Chinese Academy of Sciences, Lanzhou 730000, China*

^b*School of Nuclear Science and Technology, University of Chinese Academy of Sciences, Beijing 100049, China*

^c*Joint Department for Nuclear Physics, Lanzhou University and Institute of Modern Physics, Chinese Academy of Sciences, Lanzhou 730000, China*

^d*Research Center for Nuclear Physics, Osaka University, Ibaraki, Osaka 567-0047, Japan*

^e*RIKEN Nishina Center, Wako, Saitama 351-0198, Japan*

Abstract

A charged particle array, named MATE-PA, which serves as an auxiliary detector system to the Multi-purpose Active-target Time projection chamber for nuclear astrophysical and exotic beam Experiments (MATE) has been constructed. The array is composed of twenty single-sided strip-silicon detectors, covering around 10% of the solid angle. It is dedicated for the detection of reaction-induced charged particles which penetrate the MATE active volume. The performance of MATE-PA has been experimentally studied using an alpha source, and a 36-MeV ^{14}N beam injected into the chamber of MATE, filled with a mixture gas of 95% ^4He and 5% CO_2 under the pressure of 500 mbar, at the Radioactive Ion Beam Line in Lanzhou (RIBLL). The results demonstrate good separation of light charged particles with the forward double-layer silicon detectors of MATE-PA. The energy resolution of the Si detectors was deduced to be about 1% (σ) for an energy loss of about 10 MeV by the α particles. The inclusion of MATE-PA helps improve particle identification, and increases the

*The MATE Collaboration

*Corresponding author

Email addresses: zhangzc@impcas.ac.cn (Z. C. Zhang), zhangningtao@impcas.ac.cn (N. T. Zhang), onghjin@impcas.ac.cn (H. J. Ong)

dynamic range for the kinetic energy of charged particles, in particular that of α particles up to about 15 MeV.

Keywords: Silicon detector array, Active target, Time Projection Chamber

1. Introduction

Advances in the techniques for providing radioactive-isotope (RI) beams, and the constructions of high-intensity heavy-ion accelerator facilities [1, 2, 3, 4, 5] worldwide have opened up vast opportunities to experimentally study and understand nuclei far removed from the beta-stability line [6, 7, 8] as well as nuclear reactions relevant to astrophysics. In an experiment that uses a reaction target, the selection of a target of appropriate material or phase (solid, liquid, or gas), as well as thickness is crucial to ensure luminosity, and to achieve the intended physical goals. Since the rates of RI beams are usually several orders of magnitude lower than those of stable beams, for nuclear spectroscopy in which charged particle(s) is(are) measured, it is essential to employ sufficiently thick reaction targets while attaining moderate energy resolution. Such requirements, however, are usually hard to be fulfilled with ordinary solid or liquid targets, since uncertainty in the reaction vertices and energy straggling will impair the resolution.

The active-target time projection chamber (TPC) [9, 10] with a typical reaction gas thickness of 10 – 100 mg/cm² provides high luminosity necessary for nuclear spectroscopy with RI beams with little or moderate loss of resolution. Since the reaction gas in an active-target TPC also serves as the detector medium, the reaction vertices of reaction-induced charged particles can be determined through tracking by the TPC. Because of these advantages, scores of active-target TPCs [11, 12, 13, 14, 15, 16, 17, 18, 19] have been constructed for experiments [20, 21, 22, 23] with RI beams. Recently, a prototype active-target TPC with 1000-channel readouts named Multi-purpose Active-target Time projection chamber for nuclear astrophysical and exotic beam Experiments (MATE-1000) [24] was developed at the Institute of Modern Physics of the Chinese

Academy of Sciences (IMP-CAS), and applied to $^{12}\text{C}+^{12}\text{C}$ fusion reaction measurement at stellar energies [24], and the energies above Coulomb barrier [25]. Building on the earlier success, a larger version of MATE with about 4000-
30 channel readouts, denoted as MATE-4000 hereafter, has been constructed. The sensitive volume of MATE-4000 is $300(\text{L})\times 300(\text{W})\times 200(\text{H})\text{ mm}^3$. To detect reaction-induced charged particles that penetrate the MATE active volume, a charged particle detector array, named MATE-PA (MATE Particle detector Array), consisting of twenty single-sided strip silicon detectors was designed and
35 constructed. MATE-4000, as shown in Fig.1(a), has been commissioned using a ^{14}N beam incident on ^4He , and employed in an experiment to measure inelastic alpha scattering of ^{11}C to scrutinize the possible $Z = 6$ magic number [26] on the proton-rich side.

In this paper, we report on the construction and performance test of MATE-
40 PA. In Sec. 2, the design concept, geometry and readout electronics of the array are described. To assess the performance of the detector array, an experiment using $^{14}\text{N}+^4\text{He}$ induced reactions has been performed. Monte Carlo simulations are also performed to estimate the geometrical acceptance of MATE-PA. Details of the experiment, as well as the experimental and simulation results are given
45 in Sec. 3. The prospect of experiments with MATE-4000 in combination with MATE-PA are also presented. A conclusion and the future prospects are given in Sec. 4.

2. Charged Particle Detector Array for MATE

In this section, the design concept and specifications of MATE-PA are pre-
50 sented. The array was designed to achieve the largest possible angular coverage within MATE-4000. Detailed descriptions of MATE-4000 and its performance will be provided in another paper.

2.1. Detector array

The particle detector array consists of twenty single-sided strip silicon detec-
55 tors, produced by Hamamatsu Photonics (Serial Nos. S10938-6734 and S10938-

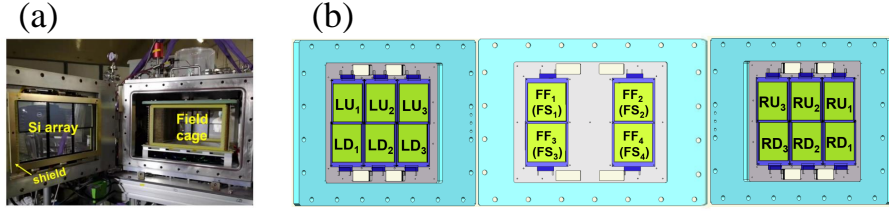


Figure 1: (a) Side view of MATE-4000 with the constructed silicon detector array. The TPC field cage (sensitive area) is placed at the center of the chamber, with twenty silicon detectors mounted on the flanges around it. (b) Layout of the silicon detector array, seen from the beam direction. The side flanges have been tilted for clarity. See text for detailed descriptions of the assignments.

6735), mounted in a single-layer 2×3 matrix on the two side walls, and a double-layer 2×2 matrix on the front wall of the target chamber. Each silicon detector has eight strips with strip widths of 11.275 mm, strip gaps of 0.1 mm, and a sensitive area of $91 \times 91 \text{ mm}^2$; the size of one silicon is 100×100 mm². The side silicons have a nominal thickness of 600 μm , while the front and rear forward silicons have thicknesses of 150 μm and 600 μm , respectively. The upper (lower) rows of the right- and left-side silicon detectors are labeled RU_i (RD_i) and LU_i (LD_i), respectively, where the subscript i indicates 1, 2, and 3. The forward detectors consist of 2 layers of Si detectors, labeled as FF_j and FS_j , respectively, where the subscript j indicates 1, 2, 3, and 4 as shown in Fig.1(b). For simplicity and to lower the risk of electric discharges, we mounted the silicon detectors close to the flanges. The distance from the RU_i (RD_i) and LU_i (LD_i) Si detectors to the field cage was set at 13.35 cm (14.00 cm), while that from FF_j (FS_j) was 17.80 cm (19.15 cm). The silicon detector array covers about 10.6% of the total (4π) solid angle in the laboratory frame, assuming that the reaction point is at the center of the TPC.

The purpose of choosing strip silicon detectors with moderately large strip widths, instead of large area single-channel or micro-strip silicon detectors, is to achieve sufficient energy resolution while keeping the readout channels at a manageable number. The current strip width is sufficient since the silicon

detector array will be used together with the TPC, which can provide track information, and the maximum rate of particles hitting the silicon detectors is expected to be of the order of a few hundreds per second.

To protect the Si detectors from possible electric discharge, a layer of electrostatic shield (as shown in Fig.1(a)) is placed between the MATE field cage and each side of the Si array. The shields were made by soldering Cu-Be wires of a diameter of $100\text{ }\mu\text{m}$ at a constant distance of 1 cm on the copper-clad surface of a glass epoxy frame. Electrical grounding is achieved by connecting the shields to the vacuum chamber. Since no electric discharge was observed during the commissioning experiment, the distances will be optimized for future experiments to improve geometrical acceptance. For instance, the geometrical acceptance can be increased by about two times by reducing the distances between the silicon detectors and the field cage from the current distance (around 15 cm) to 5 cm.

2.2. Electronics and data acquisition system

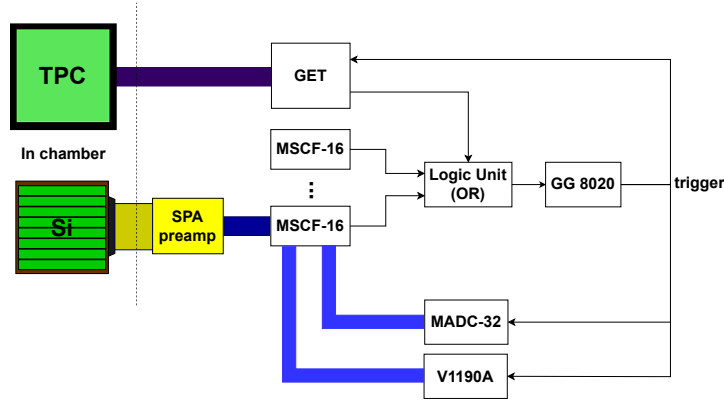


Figure 2: Typical electronic circuit diagram for the Si detectors.

The output signals of the silicon detectors are fed to 16-channel integrated charge-sensitive preamplifiers, which were designed at China Institute of Atomic Energy. The preamplifier, named Smart PreAmplifier (SPA) [27], was designed as a compact and low-cost preamplifier with a fast response and a low power con-

95 sumption. Its smaller volume allows it to be placed closer to the detectors, thus
 reducing environmental noise, and enabling it to achieve similar performance to
 other commercial preamplifier modules. Due to the limited space in the MATE
 chamber, the SPA modules are mounted on the outside of the flanges. Every six-
 teen readout signals from a SPA module are fed to a Mesytec MSCF-16 module,
 100 which includes 16-channel shaping and timing filter amplifiers, as well as con-
 stant fraction discriminators, before being fed to an analog-to-digital converter
 (ADC; Mesytec MADC-32 module). The timing signals from the MSCF-16
 modules are sent to a time-to-digital converter (TDC; CAEN V1190A module).
 A typical electronic circuit diagram is given in Fig. 2. The VME and GET (Gen-
 105 eral Electronics for TPC) [28, 29] based data acquisition system are employed
 for the data readout from the silicon and TPC detectors, respectively. Since the
 GET system acquires at a much slower rate (around 100 Hz for MATE), only
 the reaction events are selected to trigger the GET acquisition. In the current
 experiment, the OR signals from MSCF-16 modules and the GET system are fed
 110 to a gate generator (ORTEC GG8020) to provide the gate signals for VME and
 GET systems. Therefore, both DAQ devices start simultaneously and operate
 at the same rate.

3. Experiment

To evaluate the performance of the Si detector array, we have performed
 115 an experiment at the Radioactive Ion Beam Line in Lanzhou (RIBLL) [30, 31]
 at the Heavy Ion Research Facility in Lanzhou (HIRFL) [32, 33], operated by
 the IMP-CAS. A ^{14}N primary beam with an energy of 117.6 MeV provided
 by the Sector Focusing Cyclotron (SFC) was transported to RIBLL. To reduce
 the energy of ^{14}N so as to stop it in the TPC chamber, a 39.2- μm - and a
 120 60.6- μm -thick Al plates were placed at the momentum-dispersive focal plane
 C1 and at the final achromatic focal plane T2, respectively. The resulted ^{14}N
 beam with a total energy of about 36 MeV and an intensity of 10^5 pps was
 injected into the gas chamber of TPC, which was filled with a mixture gas of

95% ^4He and 5% CO_2 at 500 mbar; the mixture gas acts as the target as well as
 125 the detection medium. Charged particles generated by reactions between ^{14}N
 and the target nuclei were tracked and detected by the TPC, while part of the
 charged particles that penetrate the TPC were detected by the Si detectors.
 Data taking was performed using mainly the Si \cup TPC trigger. To prevent
 the beam from triggering the TPC, the TPC sensitive area was divided into two
 130 regions: a low-gain region with a width of ± 1.7 cm around the beam axis for the
 detection of beam particles, and high-gain regions on both sides for detection
 of reacted particles and TPC trigger generation.

For simplicity, the outputs of every four neighbouring channels of the Si
 detectors on the left and right sides were summed into one channel, which
 135 reduced the electronic readout channels without greatly affecting the energy
 resolution. Energy calibration for all Si detectors were conducted using a triple-
 nuclide alpha source, consisting of ^{239}Pu (5.147 MeV), ^{241}Am (5.486 MeV) and
 ^{244}Cm (5.805 MeV), prior to the experiment. The typical energy resolution is
 about $0.8\%(\sigma)$ at around 5.5-MeV alpha particle energy.

140 3.1. Particle identification

3.1.1. Forward region

The reaction-induced charged particles emitted in the forward direction were
 detected by the FF and FS silicon detectors. Figure 3(a) shows a typical
 particle-identification plot obtained from the measured energy deposit in the
 145 first (ΔE_{FF}) and second layer (ΔE_{FS}) of the forward silicon detectors. Three
 different loci corresponding to protons, deuterons and α particles are clearly
 seen. Here, we have eliminated overflow events and events due to accidental
 triggers taking into consideration the tracking information from the TPC.

To better understand the data, simulations using the MATEROOT pro-
 150 gram [34] were performed assuming $^4\text{He}(^{14}\text{N}, \text{p})$, $^4\text{He}(^{14}\text{N}, \text{d})$ and $^4\text{He}(^{14}\text{N}, \alpha)$
 reactions, and taking into consideration the full geometry of the detector setup,
 the incident ^{14}N beam energy, and the $^4\text{He} + \text{CO}_2$ mixture gas in the TPC
 chamber. MATEROOT is a FairRoot [35]-based data analysis and simulation

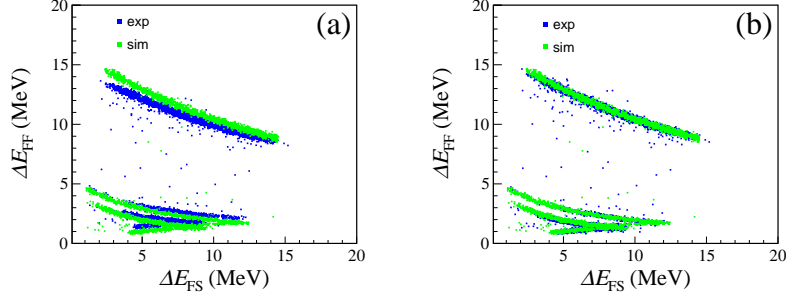


Figure 3: (a) ΔE - E plot obtained with the forward silicon detectors for charged particles induced by the ${}^4\text{He}+{}^{14}\text{N}$ reaction. The blue and green points represent experimental and simulated data, respectively. The axes are calibrated using a triple-nuclide α source. (b) ΔE - ΔE plot after re-calibration, taking into consideration the penetration point of protons.

platform, built on CERN's open source data analysis software ROOT [36] and
 155 the GEANT4 simulation framework [37], developed specifically for experiments
 with MATE. Results of the simulations (in green) are compared to the exper-
 imental data (in blue) in Fig. 3(a). Deviations between the experimental and
 simulation data are observed, which are likely to arise from insufficient energy
 calibration and inappropriate extrapolation along the energy-deposit axes. To
 160 eliminate the deviations, we consider the turnaround point of the proton locus,
 which correspond to protons that penetrate the second-layer silicon, in addi-
 tion to the triple-alpha-source data. The turnaround point was determined by
 searching for the crossing between two curves, obtained by fitting separately the
 loci for protons that penetrated and stopped in the second-layer silicon. The
 165 four data points, which include the turnaround point and the three data points
 from the triple-alpha source, were used to re-calibrate the energy-deposit axes.
 The resultant experimental loci after re-calibration are shown together with the
 simulation data in Fig. 3(b). The energy resolution of the Si detectors was
 deduced to be about 1% (σ) for an energy loss of about 10 MeV by the α parti-
 170 cles. The results demonstrate sufficient particle identification for light-charged
 particles. To further discriminate protons from energetic deuterons that punch
 through both silicon layers, it is necessary to replace the second-layer silicon

by a thicker detector, e.g. CsI(Tl) or GAGG (Gadolinium Aluminium Gallium Garnet).

175 3.1.2. Side region

Most of the light-charged particles that penetrate the TPC and head towards the side silicons stopped in the single-layer silicon detectors under the current experimental condition. Figure 4 shows a typical scattering event recorded by the detector. The z axis in Fig. 4(a) is defined as the beam axis, while the
180 y axis is the axis perpendicular to the beam direction. $z = 0$ cm represents the upstream side of the field cage, or the entrance of the TPC sensitive region for the incident beam. The rectangles at the top and two sides of the figure represent strips of silicon detectors. The same event in the x (drift direction)- z plane is shown in Fig. 4(b). The recoil α particle and the residual ^{14}N particle
185 are clearly observed simultaneously; the α particle penetrates the TPC sensitive area, and hits the highlighted group of strips (in yellow color), while the ^{14}N particle is stopped in the sensitive area. The charge and track information of the incident ^{14}N beam particle for this reaction were not recorded because of the space charge effect at the beam region with low gain.

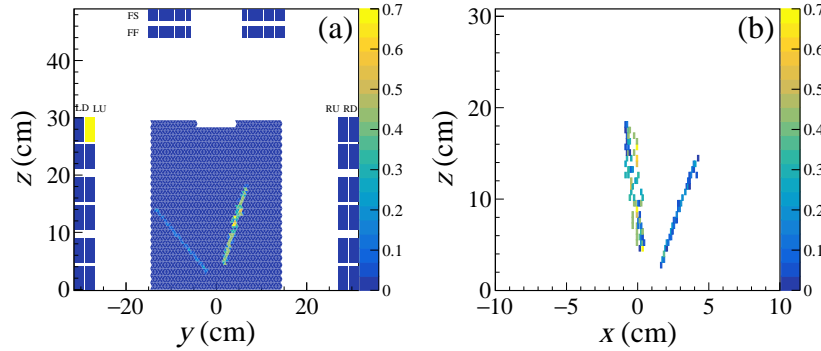


Figure 4: The trajectory of a typical scattering event on the (a) anode pad (y - z) plane, and (b) drift (x - z) plane. The z axis is the beam direction.

190 For these events, particle identification (PID) can be performed using the charge (ΔE_{TPC}) and the track length (denoted as L) obtained with the TPC, as

well as the energy deposit in the side silicons (ΔE_{Si}). The ΔE_{TPC} values were calibrated using the energy-loss curves simulated by the GEANT4 program. Typical $\Delta E_{\text{TPC}}-L$ and $\Delta E_{\text{TPC}}-\Delta E_{\text{Si+TPC}}$ scatter plots are shown in Fig. 5. For clearer identification of light and heavy particles, the ΔE_{TPC} axes of the PID plots are shown in logarithmic scale. The raw data plotted without the response of the front silicons are shown in Fig. 5(a) and (b), in which two main components can be identified roughly as particles with atomic number $Z > 2$, and light particles with $Z \leq 2$. It can be noticed from Fig. 5(a) that the expected light-charged particles with relatively high energy penetrate the TPC sensitive area from around 10 to 28 cm depending on the emitted angles, and some of them were detected by the side silicons, as shown in Fig. 5(b).

The backgrounds can be attributed mainly to TPC electronic noise and possible electrons induced by the beam particles at the beam region around the center of the TPC sensitive area along the beam direction. The former can be eliminated by limiting the number of hits on the anode pad (e.g. $10 \leq N_{\text{hits}} \leq 200$) of the TPC. The latter can be filtered out by applying geometrical constraints taking into account the kinematics of the two-body reaction, i.e. by requiring the positions of the first and last points of the trajectories to be within the high-gain region, and selecting appropriate track angles and directions for the two particles. A typical “good” event is shown in Fig. 4. After applying the above conditions, a clearer PID plot is obtained, as shown in Fig. 5(c) and (d). The backgrounds, especially the low ΔE_{TPC} components, are removed, resulting in a clear separation between ^{14}N and α particles. For the α particles that stopped in the TPC as shown in Fig. 5(c), the energies down to a few hundred keV could be detected, which is consistent with the MATE-1000 result[24]. Thanks to MATE-PA, the detection energy range is extended to about 15 MeV for α particles as shown in Fig. 5(d). Protons and deuterons were barely detected due to insufficient gain of TPC in this experiment. A clump below the ^{14}N band at around $L = 20$ cm in Fig. 5 (a) and (c) is due to a malfunctioning channel in the GET electronics, which resulted in quenched collected charges in a region close to the beam.

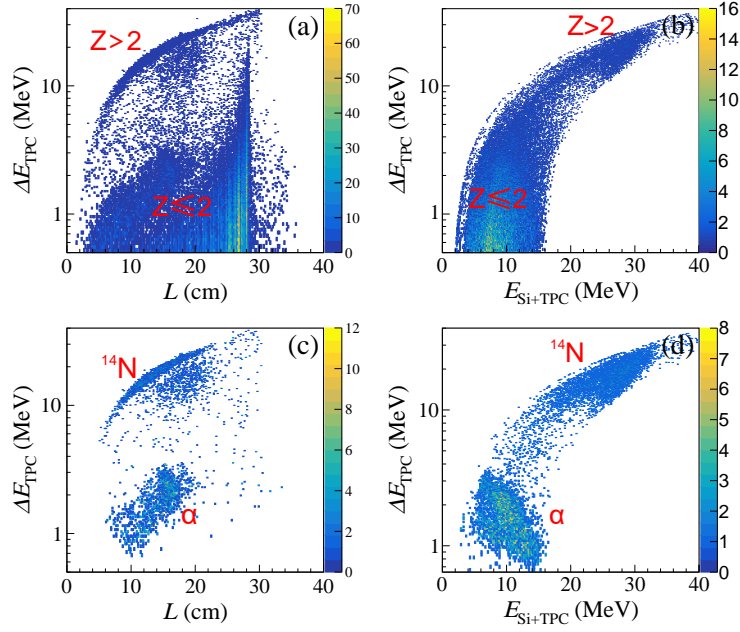


Figure 5: (a) Scattering plot of collected charge versus length of charged particles in the TPC, denoted as L . (b) ΔE - E plot for ^{14}N and α particles measured with TPC (ΔE_{TPC}) and silicon (ΔE_{Si}). (c)(d) Similar plots after applying various conditions such as number of hits on the TPC anode pad, geometrical conditions, etc. For details, see text.

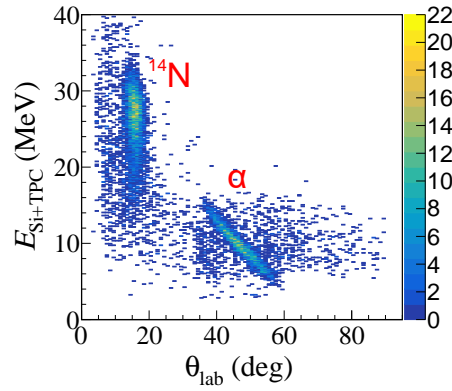


Figure 6: Correlation between the energy deposit in silicon and the angles of the particles obtained from Fig. 5(d).

The results demonstrate feasible identification and separation of scattered light particles and residual heavy particles using MATE-PA incorporating the tracking information obtained with the TPC. It is worth mentioning that thanks to the tracking information, the angles of the particles can also be extracted as shown in Fig. 6, which are useful for further analysis to refine the particle identification.

For low energy charged particles that stopped in the TPC, one has to rely on the range information for particle identification. Another good alternative is to insert the TPC into a solenoid or dipole magnet, and identify particles based on their different curved paths in the magnetic field [14].

3.2. Geometrical acceptance

For experiments that require measurements of absolute differential cross sections, it is essential to determine the solid angle or geometrical acceptance of the detectors. To estimate the geometrical acceptance, simulations using MATEROOT were performed, taking into account the full geometrical setup, incident beam energy, medium gas, as well as the energy deposit of the beam and reaction-induced charged particles in the detectors. For thick-target experiments where the reaction energy changes drastically as the beam particles travel along the TPC, it is essential to iterate the geometrical acceptance simulation taking into consideration the determined differential cross section. For simplicity, however, we assume an isotropic alpha scattering in the present work.

For reactions within a very small range of excitation energy, geometrical acceptance can be represented as a function of polar angle in center-of-mass system. The simulated geometrical acceptance of the prototype MATE-PA for the $^{14}\text{N}+^4\text{He}$ elastic scattering is shown in Fig. 7(a). The geometrical acceptance ϵ is defined as the ratio of silicon responses (total number of responses of 0 or 1 per reaction event) to the number of reaction events generated within a subtended polar angle $[\theta - \Delta\theta, \theta + \Delta\theta]$, where θ is the polar angle, and $2\Delta\theta$ is its bin size. Only the events where TPC responded to recoil α particles ($L > 5$ cm) were considered. Here, we have assumed a uniform distribution of

reaction vertices within the active volume of the TPC, and the reaction region is limited to the domain $z = [0, 10]$ cm. For a more intuitive understanding, the geometrical acceptance and the solid angle (in unit steradian) are shown as functions of angle polar angle in the laboratory system in Fig. 7(b) by the left and right axes, respectively. The angular dependence of the geometrical acceptance arises mainly from the layout of the silicon detectors.

To evaluate the dependence of the geometrical acceptance on the reaction vertex position, we divided the TPC sensitive area into ten parts along the z axis. For each part of the sensitive area, we obtained angle-integrated geometrical acceptance. The simulated result for the $^{14}\text{N}+^4\text{He}$ elastic scattering is shown in Fig. 7(c), in which the shaded region is the TPC sensitive region.

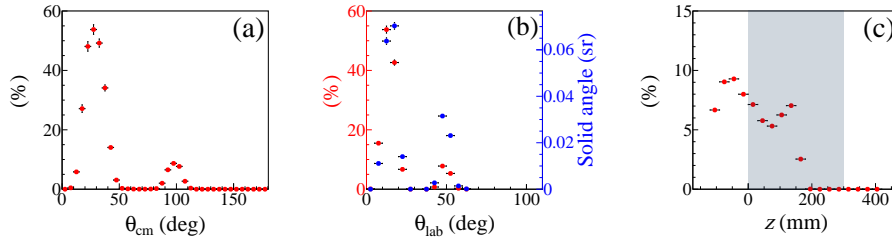


Figure 7: (a) Geometrical acceptance ϵ of MATE-PA for α particles induced by the $^4\text{He}(^{14}\text{N},\alpha)^{14}\text{N}$ reaction at different center-of-mass angles. The ^{14}N beam energy at the entrance of the TPC chamber was about 36 MeV. (b) Geometrical acceptance (left axis) and solid angle in unit steradian (right axis) of the Si array at different laboratory angles. (c) Geometrical acceptance for different reaction vertex positions along the beam axis; the shaded region is the TPC sensitive area.

The average total geometrical acceptance is estimated to be about 6.0% for the $^4\text{He}(^{14}\text{N},\alpha)^{14}\text{N}$ reaction. It is important to note that the energy of the ^{14}N beam particles decreases quickly, and no reaction occurs at the end part of the sensitive area. This leads to a reduction in the overall geometrical acceptance. The actual geometrical acceptance, however, is expected to be larger. Based on the analysis of the experimental data, some of the reaction events occurring at the so-called “dead region” between the gas entrance window and the field cage were also recorded. Therefore, in the present simulation, we have also

expanded the reaction vertex position from the TPC sensitive area to the whole gas chamber. The results show that the reactions occurring near the front of the TPC sensitive area contribute a sizable geometrical acceptance. Hence, MATE and MATE-PA can be used to measure reactions that occur both within and outside the TPC sensitive area; moderate resolution might still be achieved with careful track reconstruction and proper track extrapolation. This aspect is very useful for thick-target experiments to measure excitation function using low-energy beam.

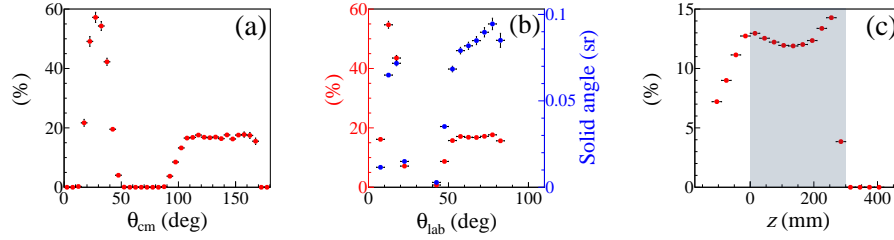


Figure 8: (a) Geometrical acceptance ϵ of MATE-PA for α particles induced by the $^4\text{He}(^{12}\text{C},\alpha)^{12}\text{C}$ reaction at different center-of-mass angles. The ^{12}C beam energy at the entrance of the TPC was about 75 MeV/nucleon. (b) Geometrical acceptance (left axis) and solid angle in unit steradian (right axis) of the Si array at different laboratory angles. (c) Geometrical acceptance for different reaction vertex positions along the beam axis; the shaded region is the TPC sensitive area.

For comparison, a simulation was also performed for the elastic alpha scattering of a ^{12}C beam with an energy of 75 MeV/nucleon incident on the TPC, filled with a mixture gas of 95% ^4He and 5% CO_2 at 500-mbar gas pressure. Results similar to those of Fig. 7 are shown in Fig. 8(a)–(d). The average total geometrical acceptance is estimated from Fig. 8(d) to be about 12.8%.

The addition of MATE-PA increases the dynamic range for the kinetic energy of charged particles, improves particle identification, and opens up broad opportunities for experiments measuring nucleon-transfer reactions, elastic and inelastic scatterings, charged-particle decay or evaporation.

4. Conclusion and future prospect

290 A prototype particle detector array consisting of twenty single-sided strip silicon detectors for use with MATE-4000 to achieve large-angle and wide energy-range measurement has been constructed. The detector system was commissioned using a 36-MeV with a 10^5 -pps ^{14}N beam incident on MATE-4000, filled with a 500-mbar mixture gas of 95% ^4He and 5% CO_2 at HIRFL-RIBLL. The
295 test results demonstrate good separation of light charged particles with the forward double-layer silicon detectors of MATE-PA. The energy resolution of the Si detectors was deduced to be about 1% (σ) for an energy loss of about 10 MeV by the α particles. Combining with MATE-PA, MATE-4000 will open up opportunities for experiments in nuclear astrophysics and RI beam physics in
300 the near future.

Recently, the readout cables of MATE-PA have been replaced by kapton ribbon cables to improve flexibility and work efficiency. The use of ribbon cables also helps improve environmental noise. In terms of the readout electronics, we use SPA and MSCF, incorporating a VME-based ADC for the data acquisition
305 at present. We plan to migrate the General Electronics for TPCs (GET) system, which is used for the readout of the TPC signals, in the near future. An upgrade of MATE-PA with additional detectors such as CsI(Tl) or GAGG is also under consideration to accommodate a wide variety of experiments.

Acknowledgement

310 The authors thank the accelerator operators for the stable beams throughout the experiment. This work was partially supported by the National Natural Science Foundation of China under Contracts Nos. 12175280 and 12250610193, and the National Key R & D Program of China (2016YFA0400500). H.J. Ong and X.D. Xu acknowledges the support of the CAS “Light of West China” Program. Z.C. Zhang acknowledges the support of the Natural Science Foundation
315 of Gansu under Contract No. 23JRRA676.

References

- [1] H. Geissel, H. Weick, M. Winkler, et al., The Super-FRS project at GSI, Nucl Instrum Meth B 204 (2003) 71–85, <https://www.sciencedirect.com/science/article/pii/S0168583X02018931>.
320
- [2] D. J. Morrissey, Status of the FRIB project with a new fragment separator, Journal of Physics: Conference Series 267 (1) (2011) 012001, <https://doi.org/10.1088/1742-6596/267/1/012001>.
- [3] T. Kubo, D. Kameda, H. Suzuki, et al., BigRIPS separator and ZeroDegree spectrometer at RIKEN RI Beam Factory, Progress of Theoretical and Experimental Physics 2012 (1) (2012) 03C003, <https://doi.org/10.1093/ptep/pts064>.
325
- [4] L. N. Sheng, X. H. Zhang, J. Q. Zhang, et al., Ion-optical design of High energy FRagment Separator (HFRS) at HIAF, Nucl Instrum Meth B 469 (2020) 1–9, <https://www.sciencedirect.com/science/article/pii/S0168583X20300859>.
330
- [5] J. Yang, J. Xia, G. Xiao, et al., High intensity heavy ion accelerator facility (hiaf) in china, Nuclear Instruments and Methods in Physics Research Section B: Beam Interactions with Materials and Atoms 317 (2013) 263–265, <https://www.sciencedirect.com/science/article/pii/S0168583X13009877>.
335
- [6] P. Hansen, B. Sherrill, Reactions and single-particle structure of nuclei near the drip lines, Nuclear Physics A 693 (1) (2001) 133–168, <https://www.sciencedirect.com/science/article/pii/S0375947401011046>.
- [7] T. Nakamura, H. Sakurai, H. Watanabe, Exotic nuclei explored at in-flight separators, Progress in Particle and Nuclear Physics 97 (2017) 53–122, <https://www.sciencedirect.com/science/article/pii/S0146641017300522>.
340

- [8] M. Pfützner, I. Mukha, S. Wang, Two-proton emission and related phenomena, *Progress in Particle and Nuclear Physics* 132 (2023) 104050, <https://www.sciencedirect.com/science/article/pii/S0146641023000315>.
345
- [9] D. R. Nygren, A Time Projection Chamber: 1975, in: 1975 PEP Summer Study, 1975, pp. 126–133.
- [10] D. Bazin, T. Ahn, Y. Ayyad, et al., Low energy nuclear physics with active targets and time projection chambers, *Progress in Particle and Nuclear Physics* 114 (2020) 103790, <https://www.sciencedirect.com/science/article/pii/S0146641020300375>.
350
- [11] C. E. Demonchy, W. Mittig, H. Savajols, et al., MAYA, a gaseous active target, *Nucl Instrum Meth A* 573 (1) (2007) 145–148, <https://www.sciencedirect.com/science/article/pii/S0168900206022558>.
355
- [12] S. Ota, H. Tokieda, C. S. Lee, et al., CNS active target (CAT) for missing mass spectroscopy with intense beams, *Nucl Chem* 305 (3) (2015) 907–911, <https://doi.org/10.1007/s10967-015-4130-5>.
- [13] W. Mittig, S. Beceiro-Novo, A. Fritsch, et al., Active Target detectors for studies with exotic beams: Present and next future, *Nucl Instrum Meth A* 784 (2015) 494–498, <https://www.sciencedirect.com/science/article/pii/S0168900214012054>.
360
- [14] J. Bradt, D. Bazin, F. Abu-Nimeh, et al., Commissioning of the Active-Target Time Projection Chamber, *Nucl Instrum Meth A* 875 (2017) 65–79, <https://www.sciencedirect.com/science/article/pii/S0168900217309683>.
365
- [15] T. Furuno, T. Kawabata, H. J. Ong, et al., Performance test of the MAIKo active target, *Nucl Instrum Meth A* 908 (2018) 215–224, <https://www.sciencedirect.com/science/article/pii/S0168900218309951>.
- [16] E. Koshchiy, G. Rogachev, E. Pollacco, et al., Texas Active Target (TexAT) detector for experiments with rare isotope beams, *Nucl Instrum Meth A*
370

957 (2020) 163398, <https://www.sciencedirect.com/science/article/pii/S0168900220300073>.

- 375 [17] J. Y. Xu, L. Q. T, Y. L. Y, et al, Performance of a small AT-TPC prototype, Nucl Sci Tech 29 (2018) 263–265, <https://doi.org/10.1007/s41365-018-0437-6>.
- [18] L. S. Yang, J. Y. Xu, Q. T. Li, et al, Performance of the CAT-TPC based on two-dimensional readout strips, Nucl Sci Tech 32 (2021) 85, <https://doi.org/10.1007/s41365-021-00919-6>.
- 380 [19] H. Wu, Y. Wang, et al., Machine learning method for ^{12}C event classification and reconstruction in the active target time-projection chamber, Nucl Instrum Meth A 1055 (2023) 168528, <https://www.sciencedirect.com/science/article/pii/S0168900223005181>.
- 385 [20] T. Furuno, T. Kawabata, S. Adachi, et al., Neutron quadrupole transition strength in ^{10}C deduced from the $^{10}\text{C}(\alpha, \alpha')$ measurement with the MAIKo active target, Phys. Rev. C 100 (2019) 054322, <https://link.aps.org/doi/10.1103/PhysRevC.100.054322>.
- [21] J. Bishop, C. E. Parker, G. V. Rogachev, et al., Neutron-upscattering enhancement of the triple-alpha process, Nature Communications 13 (2022) 2151, <https://doi.org/10.1038/s41467-022-29848-7>.
- 390 [22] J. Bishop, G. V. Rogachev, S. Ahn, et al., First observation of the $\beta 3\alpha$ decay of ^{13}O via β -delayed charged-particle spectroscopy, Phys. Rev. Lett. 130 (2023) 222501, <https://link.aps.org/doi/10.1103/PhysRevLett.130.222501>.
- 395 [23] S. Giraud, J. C. Zamora, R. G. T. Zegers, et al, β^+ gamow-teller strengths from unstable ^{14}O via the $(d, ^2\text{He})$ reaction in inverse kinematics, Phys. Rev. Lett. 130 (2023) 232301, <https://link.aps.org/doi/10.1103/PhysRevLett.130.232301>.

- [24] Z. C. Zhang, X. Y. Wang, T. L. Pu, et al., Studying the heavy-ion fusion
 400 reactions at stellar energies using Time Projection Chamber, Nucl Instrum
 Meth A 1016, <https://doi.org/10.1016/j.nima.2021.165740> (2021).
- [25] X. Y. Wang, N. T. Zhang, Z. C. Zhang, et al., Studies of the 2α and 3α
 channels of the $^{12}\text{C}+^{12}\text{C}$ reaction in the range of $E_{\text{c.m.}}=8.9$ MeV to 21 MeV
 using the active target Time Projection Chamber, Chinese Phys. C 46 (10)
 405 (2022) 104001, <https://dx.doi.org/10.1088/1674-1137/ac7a1d>.
- [26] D. T. Tran, H. J. Ong, G. Hagen, et al., Evidence for prevalent $Z = 6$ magic
 number in neutron-rich carbon isotopes, Nature Communications 9 (2018)
 1594, <https://doi.org/10.1038/s41467-018-04024-y>.
- [27] D. X. Wang, C. J. Lin, L. Y., et al., Compact 16-channel integrated charge-
 410 sensitive preamplifier module for silicon strip detectors, Nucl Sci Tech 31 (5)
 (2020) 48, <https://doi.org/10.1007/s41365-020-00755-0>.
- [28] J. Giovinazzo, T. Goigoux, S. Anvar, et al., GET electronics samples data
 analysis, Nucl Instrum Meth A 840 (2016) 15–27, <https://doi.org/10.1016/j.nima.2016.09.018>.
- 415 [29] E. C. Pollacco, G. F. Grinyer, F. Abu-Nimeh, et al., GET: A generic elec-
 tronics system for TPCs and nuclear physics instrumentation, Nucl Instrum
 Meth A 887 (2018) 81–93, <https://doi.org/10.1016/j.nima.2018.01.020>.
- [30] S. Zhi-yu, Z. Wen-long, G. Zhong-yan, et al., Separation and Identification
 420 of Isotopes Produced from $^{20}\text{Ne}+\text{Be}$ Reaction by Radioactive Ion Beam
 Line in Lanzhou, Chinese Physics Letters 15 (11) (1998) 790, <https://dx.doi.org/10.1088/0256-307X/15/11/004>.
- [31] Z. Y. Sun, W. L. Zhan, Z. Y. Guo, RIBLL, the radioactive ion beam line
 in Lanzhou, Nucl Instrum Meth A 503 (3) (2003) 496–503, [https://doi.org/10.1016/S0168-9002\(03\)01005-2](https://doi.org/10.1016/S0168-9002(03)01005-2).
 425

- [32] J. W. Xia, W. L. Zhan, B. W. Wei, et al., The heavy ion cooler-storage-ring project (HIRFL-CSR) at Lanzhou, Nucl Instrum Meth A 488 (1) (2002) 11–25, [https://doi.org/10.1016/S0168-9002\(02\)00475-8](https://doi.org/10.1016/S0168-9002(02)00475-8).
- 430 [33] W. L. Zhan, H. S. Xu, Z. Y. Sun, et al., Present Status of HIRFL In Lanzhou, International Journal of Modern Physics E 15 (2006) 1941–1956, <https://doi.org/10.1142/S0218301306005526>.
- [34] L. Li, Z. C. Zhang, N. T. Zhang, et al., MATEROOT: A Simulation and Analysis Tool for Experiments with MATE, in preparation.
- 435 [35] M. Al-Turany, D. Bertini, R. Karabowicz, et al., The fairroot framework, Journal of Physics: Conference Series 396 (2) (2012) 022001, <https://dx.doi.org/10.1088/1742-6596/396/2/022001>.
- [36] R. Brun, F. Rademakers, ROOT — An object oriented data analysis framework, Nucl Instrum Meth A 389 (1) (1997) 81–86, <https://www.sciencedirect.com/science/article/pii/S016890029700048X>.
- 440 [37] S. Agostinelli, J. Allison, K. Amako, et al., Geant4—a simulation toolkit, Nucl Instrum Meth A 506 (3) (2003) 250–303, <https://www.sciencedirect.com/science/article/pii/S0168900203013688>.